Journal of Theoretical and Applied Mechanics, Sofia, Vol.55 (2025) pp. 486-502
FLUID MECHANICS

MAGNETOHYDRODYNAMICS FLOW IN DOUBLE-LID L-SHAPED CAVITY WITH LOCAL REFINEMENT

EBUTALIB ÇELIK[1*], MERVE GURBUZ-CALDAG[2]

[1] *Department of Computer Technologies, Çanakkale Onsekiz Mart University, Çanakkale, Turkey*

[2] *Department of Mathematics, TED University, Ankara, Turkey*

[Received: 12 July 2025. Accepted: 8 December 2025]

doi: https://doi.org/10.55787/jtams.25.55.4.485

ABSTRACT: This study presents new insights into structures of magnetohydrodynamics flow in a double lid-driven L-shaped cavity under an oriented magnetic field. The governing equations are presented using the stream function-vorticity approach and solved numerically. Radial basis function-finite difference method utilizing polyharmonic splines is proposed to achieve local refinement. Flow topologies are examined for problem parameters, including the inclination angle, Hartmann number, and Reynolds number. The results indicate that as the strength of the magnetic field increases, the Lorentz force becomes the dominant factor, making the impact of the Reynolds number on flow negligible. The strength and inclination angle of the magnetic field play crucial roles in influencing the flow structure by altering the number, position, and type of critical points, and type of critical points.

KEY WORDS: Domain decomposition, L-shaped cavity, Magnetohydrodynamics (MHD) flow.

1 INTRODUCTION

Incompressible laminar flow in an L-shaped geometry problem was initially considered by Perng and Street [1]. A coupled multrigrid domain splitting method is employed to calculate the velocity-pressure form of the Navier-Stokes equation. Hriberšek and Škerget [2] showed that the boundary domain integral method (BDIM) is applicable to find solutions to flow problems in complex geometries, including an L-shaped cavity. The convection problems in an L-shaped cavity are numerically solved to investigate the heat transfer [3–7]. Moreover, the Lorentz force term is added into the convection equations to examine the impact of the magnetic field on the convection problem in an L-shaped cavity. Selimefendigil and Öztop [8] studied the effect of the magnetic field on the driven flow of nanofluid convection in an L-shaped cavity. The numerical computations are carried out for different values of

*Corresponding author e-mail: e.celik@comu.edu.tr

Hartmann, Richardson, and internal Rayleigh numbers, inclination angle of the cavity and magnetic field, solid nanoparticle volume, and aspect ratio of the cavity. It is reported that the inclination angle of the magnetic field has a significant effect on the heat transfer. The impact of the oriented magnetic field on mixed convection in hybrid nanofluid of Al2O3-Cu/Water is studied by Armaghani *et al.* [9]. It is shown that the best heat transfer is obtained when the inclination angle of the magnetic field is π. Saleem *et al.* [10] and Khan *et al.* [11] obtained numerical simulations of the heat transfer of the natural convection flow in an L-shaped cavity filled with Cu-water nanofluid using the COMSOL package. Khan *et al.* [12] considered the entropy generation and heat transfer in an L-shaped enclosure to optimize thermal system design by using the FEM and artificial neural network.

Deliceoğlu and Aydın [13] studied the flow bifurcation and eddy genesis in an L-shaped cavity with slip conditions for the top and bottom walls. Stokes and Navier-Stokes equations are solved by using a Galerkin FEM for different values of Reynolds number and the aspect ratio of the cavity. They depicted that problem parameters change the structure of the flow pattern. Moreover, they analyzed the flow pattern of the same problem taking the no-slip boundary condition for the bottom wall in [14]. Stokes equation is solved analytically using an infinite series of eigenfunctions to analyze the impact of the length of the L-shaped cavity on streamlines. Deliceoğlu *et al.* [15] investigated the utilization of topology to represent flow patterns in an L-shaped cavity with the top and bottom walls moving in the same directions. The topological behavior of the streamlines of the Stokes flow is shown in various ranges of heights of the cavity. The effects of the Reynolds number on the flow pattern in the L-shaped cavity are included by Bhopalam and Perumal [16]. Lattice Boltzmann method is applied to solve the Navier-Stokes equations for the variations of Reynolds number and the aspect ratio of the cavity. Flow structures are also depicted in the cavity with three different types of bottom wall conditions.

Various domain decomposition methods have been used in solving engineering problems. Cheng and Shaikh [17] presented the scheme based on the non-overlap domain decomposition method. They used the coarse mesh difference scheme at the interface grids and the fine mesh difference scheme at the interior mesh points. Chniti *et al.* [18] dealt with a local improvement of domain decomposition methods for 2-dimensional elliptic problems for which either the geometry or the domain decomposition presents conical singularities. Chniti [19] also studied derive appropriate second-order transmission boundary conditions near the corner used in domain decomposition methods to study the reaction diffusion problems with strong heterogeneity in the coefficients in a singular non-convex domain with Neumann and Dirichlet boundary condition.

The aforementioned studies, the flow behavior and heat transfer of nanofluids in

L-shaped cavities are considered. Analysis of flow topology is generally restricted to the Navier–Stokes or Stokes formulations in the absence of a magnetic field. In [20], the influence of a magnetic field on Stokes flow in an L-shaped cavity with a moving top lid only is examined. The convective terms are neglected due to the Stokes approximation. In contrast, the present study examines the effect of an oriented magnetic field on the flow topology in an L-shaped cavity with both the upper and lower lids in motion. Besides, the governing equations include convective terms, representing MHD flow. In this method, polyharmonic spline basis functions with polynomial augmentation are adopted, eliminating the need for shape parameters and enhancing numerical robustness. Therefore, this study makes a novel contribution to numerical modeling of MHD flows in non-convex geometries, providing new insights into lid-driven cavity dynamics under magnetic influence. This contributes to the optimization of designs in various engineering applications where such configurations are used.

2 Governing Equations of MHD Flow

The two-dimensional, time-independent flow in an L-shaped cavity filled with a viscous, incompressible, and electrically conducting fluid is considered in the presence of the oriented magnetic field. The top and bottom walls have movement in different directions ($S = -1$) or in the same direction ($S = 1$). The problem is configured in Fig. 1a. The non-dimensional MHD equations obtained by the momentum equations including Lorentz force term [21, 22] are

$$(1) \qquad \nabla \cdot \overrightarrow{u} = 0, \qquad \nabla^2 \overrightarrow{u} = \nabla p + Re(\overrightarrow{u} \cdot \nabla)\overrightarrow{u} - M^2(\overrightarrow{u} \times \overrightarrow{H}) \times \overrightarrow{H}.$$

where $\overrightarrow{u} = (u, v, 0)$ is the velocity field, p is the pressure and $\overrightarrow{H}$ is the applied magnetic field. In these equations, the nondimensional parameters are Reynolds number ($Re = lu_l/\nu$) and Hartmann number ($M = l\mu H_0(\sigma/\rho\nu)^{1/2}$), in which l, u_l and H_0,

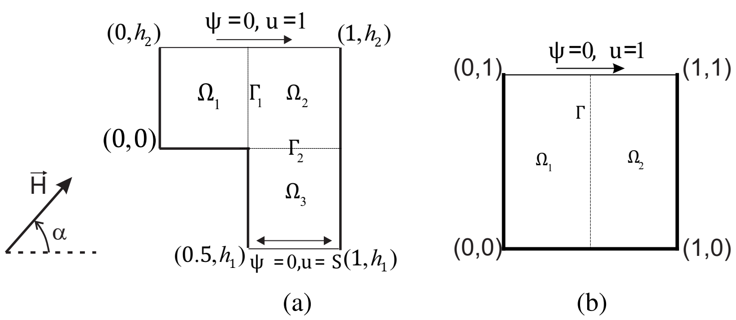

Fig. 1. Divided flow domain with boundary conditions in lids: (a) L-shaped geometry; (b) Square geometry.

ρ, ν, μ and σ are characteristic length, characteristic velocity, magnetic field intensity, density, kinematic viscosity, magnetic permeability and electrical conductivity, respectively.

Equations in (1) can be expressed in the stream function-vorticity ($\psi - \omega$) form as

$$\nabla^2\psi = -\,\omega\,, \tag{2}$$

$$\begin{aligned}\nabla^2\omega =& Re(\psi_y\omega_x - \psi_x\omega_y)\\ &+ M^2(-\sin^2\alpha\;\psi_{yy} - 2sin\alpha\cos\alpha\;\;\psi_{yx} - \cos^2\alpha\;\psi_{xx})\,,\end{aligned} \tag{3}$$

where α is the inclination angle of the magnetic field.

3 Method with local RBF

3.1 RBF-base finite difference

In the finite difference method (FDM), a partial derivative of an unknown function ($\mathcal{L}u$) at a point x_c can be calculated by using a linear combination of the values of the function at the $n-$ nearest grid locations included with x_c itself, which is given by

$$\mathcal{L}u|_{x_c} \approx \sum_{i=1}^{n} w_i u_i. \tag{4}$$

Coefficients of unknown functions w_i in (4) called the weights and are determined by using radial basis functions (RBF). The weights w_i are obtained by following the system based on the stencil $\{x_i\}_{i=1}^{n}$.

$$\underbrace{\begin{bmatrix} \varphi\left(\|x_1 - x_1\|\right) & \cdots & \varphi\left(\|x_1 - x_n\|\right) \\ \vdots & \ddots & \vdots \\ \varphi\left(\|x_n - x_1\|\right) & \cdots & \varphi\left(\|x_n - x_n\|\right) \end{bmatrix}}_{A} \begin{bmatrix} w_1 \\ \vdots \\ w_n \end{bmatrix} = \begin{bmatrix} \mathcal{L}\varphi\left(\|x_c - x_1\|\right) \\ \vdots \\ \mathcal{L}\varphi\left(\|x_c - x_n\|\right) \end{bmatrix}, \tag{5}$$

where φ is a radial basis function and, $\|.\|$ is the Euclidean distance. There are many types of RBFs which are Multiquadratics (MQ) ($\varphi = \sqrt{r^2 + \varepsilon^2}$), Inverse MQ ($\varphi = 1\Big/\sqrt{r^2 + \varepsilon^2}$), Gaussian ($\varphi = e^{-\varepsilon^2 r^2}$) and polyharmonic splines (PHS) ($\varphi = r^{2l+1}$). Some RBFs include predefined shape parameters ε that influence the system solution (5). Therefore, we focus on the usage of PHS with polynomial augmentation up to degree p. If we consider approximating differential operator $\mathcal{L}$ with PHS polynomial augmentation, the system (4) can be rearranged as follows:

$$
(6)\quad
\left[
\begin{array}{c|c}
A & \overbrace{\begin{matrix} 1 & x_1 & y_1 & \cdots & x_1^p & y_1^p \\ \vdots & \vdots & \vdots & \ddots & \vdots & \vdots \\ 1 & x_n & y_n & \cdots & x_n^p & y_n^p \end{matrix}}^{\mathbf{P}} \\
\hline
\underbrace{\begin{matrix} 1 & \cdots & 1 \\ x_1 & \cdots & x_n \\ y_1 & \cdots & y_n \\ \vdots & \iddots & \vdots \\ x_1^p & \cdots & x_n^p \\ y_1^p & \cdots & y_n^p \end{matrix}}_{\mathbf{P}^T} & 0
\end{array}
\right]
\begin{bmatrix}
\overbrace{\begin{matrix} w_1 \\ \vdots \\ w_n \end{matrix}}^{\mathbf{w}} \\
\hline
\underbrace{\begin{matrix} \zeta_1 \\ \vdots \\ \zeta_m \end{matrix}}_{\boldsymbol{\zeta}}
\end{bmatrix}
=
\left[
\begin{array}{c}
\overbrace{\begin{matrix} \mathcal{L}\varphi\left(\|x_c - x_1\|\right) \\ \vdots \\ \mathcal{L}\varphi\left(\|x_c - x_n\|\right) \end{matrix}}^{\mathcal{L}\boldsymbol{\varphi}} \\
\hline
\underbrace{\begin{matrix} \mathcal{L}1|_{x_c} \\ \mathcal{L}x|_{x_c} \\ \mathcal{L}y|_{x_c} \\ \vdots \\ \mathcal{L}x^p|_{x_c} \\ \mathcal{L}y^p|_{x_c} \end{matrix}}_{\mathcal{L}\mathbf{p_i}(x)}
\end{array}
\right],
$$

where $\mathbf{w}$ and $\mathcal{L}\boldsymbol{\varphi}$ are $n \times 1$ column vectors generated by w_i and $\mathcal{L}\varphi\left(\|x_c - x_i\|\right)$, $\mathbf{P}$ is $n \times m$ matrix containing multivariate polynomial terms of total degree less than or equal to p in each row, $\mathbf{P^T}$ is transpose of $\mathbf{P}$, $\boldsymbol{\zeta}$ and $\mathcal{L}\mathbf{p}$ are also $m \times 1$ column vectors produced by ζ and $\mathcal{L}\mathbf{p_i}(\mathbf{x_c})$. The scalar p and m express the highest degree of the polynomials $p_i(x), i = 1, 2, ...,$ and total number of polynomial terms in augmentation, respectively. The number of polynomial terms m in 2D can be evaluated as $m = \begin{pmatrix} p+2 \\ p \end{pmatrix}$. For instance, the set of multivariate polynomials is $p(x) = \left\{1, x, y, xy, x^2, y^2\right\}$ related to $p = 2$. After solving the system, we eliminate the weights $\boldsymbol{\zeta}$. The discussion on unisolvency conditions and RBF-FD weights are stated in [23–26].

3.2 Numerical Methods

We consider that L-shaped flow region consist of three sub-regions $(\Omega_1, \Omega_2, \Omega_3)$ and interfaces (Γ_1, Γ_2) as $\Omega = \Omega_1 \cup \Omega_2 \cup \Omega_3 \cup \Gamma_1 \cup \Gamma_2$ shown in Fig. 1a

$$
\begin{aligned}
\Omega_1 &= \{(x, y) : 0 < x < 0.5, 0 < y < h_2\}, \\
\Omega_2 &= \{(x, y) : 0.5 < x < 1, 0 < y < h_2\}, \\
\Omega_3 &= \{(x, y) : 0.5 < x < 1, h_1 < y < 0\},
\end{aligned}
$$

and

$$
\Gamma_1 = \{(0.5, y) : 0 < y < h_2\}, \quad \Gamma_2 = \{(x, 0) : 0.5 < x < 1\}.
$$

Step size set $h = 0.5/N$, $h_1^* = h_1/N^*$, $h_2^* = h_2/2N$ and the set of grid points is $\mathcal{N} = \mathcal{N}_1 \cup \mathcal{N}_2 \cup \mathcal{N}_3 \cup \mathcal{N}_1^* \cup \mathcal{N}_2^*$ such that

$$
\begin{aligned}
\mathcal{N}_1 &= \{(ih, jh_2^*) : 1 \le i \le N-1, 1 \le j \le 2N-1\},\\
\mathcal{N}_2 &= \{(ih, jh_2^*) : N+1 \le i \le 2N-1, 1 \le j \le 2N-1\},\\
\mathcal{N}_3 &= \{(ih, jh_1^*) : N+1 \le i \le 2N-1, 1 \le j \le N^*-1\},\\
\mathcal{N}_1^* &= \{(0.5, jh_2^*) : 1 \le j \le 2N-1\},\\
\mathcal{N}_2^* &= \{(ih, 0) : N+1 \le i \le 2N-1\},
\end{aligned}
$$

where $\mathcal{N}_1 \cup \mathcal{N}_2 \cup \mathcal{N}_3$ is related to sub-region while $\mathcal{N}_1^* \cup \mathcal{N}_2^*$ is the set of interface points. The coupled equations (2)-(3) are solved by using 5-point central difference for each sub-region $\Omega_1, \Omega_2, \Omega_3$ and RBF-enhanced F.D. for the interfaces. For detailed information about the method, see [20]. The boundary conditions for the lids and stationary walls are

$$
(7)\qquad \begin{cases} u_{i,2N}^{(I)} = 1, \psi_{i,2N}^{(I)} = 0, \; 1 \le i \le N-1 \\ v_{0,j}^{(I)} = 0, \psi_{0,j}^{(I)} = 0, \quad 1 \le j \le 2N-1 \\ u_{i,0}^{(I)} = \psi_{i,0}^{(I)} = 0, \quad 1 \le i \le N-1 \end{cases} \qquad (ih, jh_2^*) \in \mathcal{N}_1,
$$

$$
(8)\qquad \begin{cases} u_{i,2N}^{(II)} = 1, \psi_{i,2N}^{(II)} = 0, \; N+1 \le i \le 2N-1 \\ v_{2N,j}^{(II)} = 0, \psi_{2N,j}^{(II)} = 0, \; 1 \le j \le 2N-1 \end{cases} \qquad (ih, jh_2^*) \in \mathcal{N}_2,
$$

$$
(9)\qquad \begin{cases} u_{i,N^*}^{(III)} = S, \psi_{i,N^*}^{(III)} = 0, \; N+1 \le i \le 2N-1 \\ v_{2N,j}^{(III)} = \psi_{2N,j}^{(III)} = 0, \quad 1 \le j \le N^*-1 \\ v_{N,j}^{(III)} = \psi_{N,j}^{(III)} = 0, \quad 1 \le j \le N^*-1 \end{cases} \qquad (ih, jh_1^*) \in \mathcal{N}_3.
$$

The matching conditions between the sub-regions

$$
(10)\qquad \begin{cases} \psi_{0.5,j}^{(I)} = \psi_{0.5,j}^{(II)}, \; \omega_{0.5,j}^{(I)} = \omega_{0.5,j}^{(II)} \; 1 \le j \le 2N-1, (0.5, jh_2^*) \in \mathcal{N}_1^* \\ \psi_{i,0}^{(II)} = \psi_{i,0}^{(III)}, \; \omega_{i,0}^{(II)} = \omega_{i,0}^{(III)} \; N+1 \le i \le 2N-1, (ih, 0) \in \mathcal{N}_2^* \end{cases}
$$

hold at the interfaces for a continuous solution. Boundary conditions of the vorticity are derived from the Taylor expansion of the stream function, as listed in Table 1.

4 Flow Characteristic in Aspect of Topology

In addition to the computational results, the aim is also the investigation of the streamline in terms of the topological aspect along the flow. In the analysis, the term "bifurcation of the flow" refers to the transformation in the structure of the stagnation points at which the velocity components vanish. Flow patterns at the origin are determined by the standard Hamiltonian systems $\dot{x} = \dfrac{\partial \psi}{\partial y} = 0$, $\dot{y} = -\dfrac{\partial \psi}{\partial x} = 0$. In these

Table 1. Wall conditions of the vorticity for sub-regions of the cavity

Upper Wall $\{\Omega_m\}_{m=1,2}$	$\omega_{i,2N}^{(m)} = \dfrac{7\psi_{i,2N}^{(m)} - 8\psi_{i,2N-1}^{(m)} + \psi_{i,2N-2}^{(m)}}{2(h_2^*)^2} - \dfrac{3}{h_2^*}u_{i,2N}^{(m)}$
Bottom Wall	$\omega_{i,0}^{(I)} = \dfrac{7\psi_{i,0}^{(I)} - 8\psi_{i,1}^{(I)} + \psi_{i,2}^{(I)}}{2(h_2^*)^2}$
	$\omega_{i,N^*}^{(III)} = \dfrac{7\psi_{i,N^*}^{(III)} - 8\psi_{i,N^*-1}^{(III)} + \psi_{i,N^*-2}^{(III)}}{2(h_1^*)^2} - \dfrac{3}{h_1^*}u_{i,N^*}^{(m)}$
Right Wall $\{\Omega_m\}_{m=2,3}$	$\omega_{2N,j}^{(m)} = \dfrac{7\psi_{2N,j}^{(m)} - 8\psi_{2N-1,j}^{(m)} + \psi_{2N-2,j}^{(m)}}{2h^2}$
Left Wall	$\omega_{0,j}^{(I)} = \dfrac{7\psi_{0,j}^{(I)} - 8\psi_{1,j}^{(I)} + \psi_{2,j}^{(I)}}{2h^2}$
	$\omega_{N,j}^{(III)} = \dfrac{7\psi_{N,j}^{(III)} - 8\psi_{N+1,j}^{(III)} + \psi_{N+2,j}^{(III)}}{2h^2}$

systems, the linear part of $\psi = \sum_{i+j=0}^{\infty} a_{i,j}x^i y^j$ gives the types of inflow critical points. Their types depend on the determinant of the positivity of the Jacobian matrix, such that if the determinant of the Jacobian matrix $|J|$ is positive, its type is a center; if $|J| < 0$ it is a saddle, as shown in Fig. 2a.

In the case of $|J| = 0$, the critical points are degenerate, and the higher-order terms of ψ are required to decide the character of the flow patterns. In the case of zero eigenvalue with geometric multiplicity one, this refers to a simple linear degeneracy. Brøns and Hartnack [27] used the canonical transformation to classify the possible degenerate patterns and their unfoldings. It is found that the center point transforms

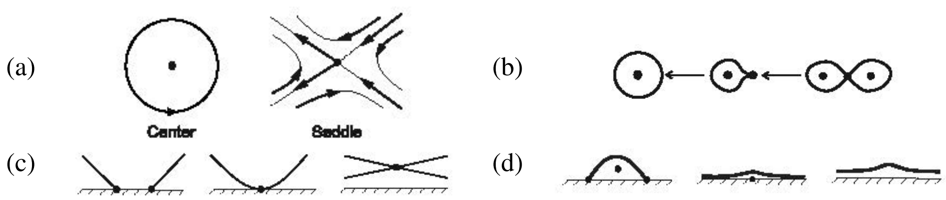

Fig. 2. Streamline topology near stagnation points.

into three critical points with a saddle and two centers or vice versa in the normal form of order 3. This bifurcation is called the cusp bifurcation (C.P) and is shown in Fig. 2b.

Near a fixed wall with a simple linear degenerate point, Hartnack [28] exhibited two kinds of bifurcation series in the normal form of order 4. The first is the formation of bubble merging (B.M), that is, two on-wall saddle points produce a heteroclinic link with a center near them. The second is the transformation to bubble creation (B.C.), in which merging occurs by the coalescing of two on-wall saddle points. These situations are physically interpreted as shown in Fig. 2c-Fig. 2d, respectively. In addition, a global bifurcation (G. B.) occurs when an off-wall saddle point has the same stream function value as a critical point on the wall. Eddy generation on side wall of cavity is expressed with S.E. abbreviation.

5 Numerical Results

In this work, the successive over-relaxation (SOR) is utilized as an iteration method to solve the system generated by the numerical method. The iteration starts with the initial values of vorticity ω^0 and stream function ψ^0. $\nabla^2\psi = -\omega$ is solved for each sub-region, then the boundary conditions in Table 1 are specified for the vorticity. The new value of the vorticity ω^{n+1} is obtained from equation (3) for $\{\Omega_i\}_{i=1,2,3}$. The same process with updated boundary conditions is applied to the interfaces $\{\Gamma_i\}_{i=1,2}$ with the specified method. The iteration continues until the con-

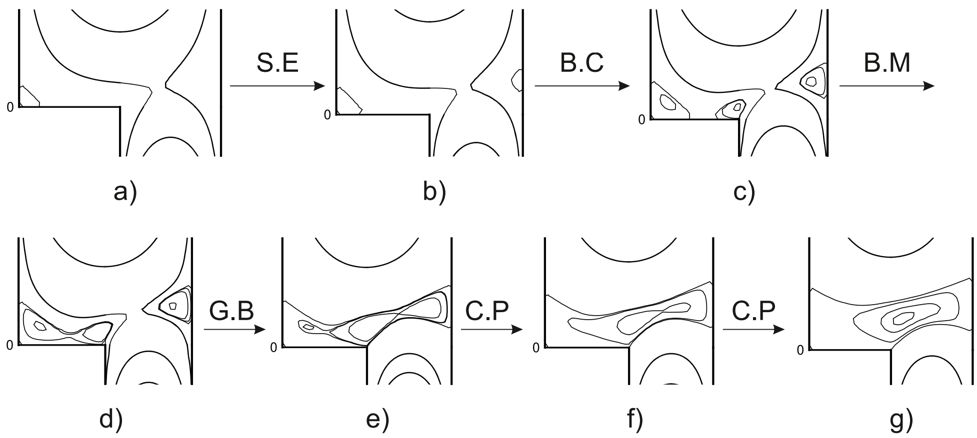

Fig. 3. A scenario of vortex formation near the step in L-shaped cavity for $S = -1$: (a) $h_1 = -0.5, h_2 = 1.2$; (b) $h_1 = -0.5, h_2 = 1.35$; (c) $h_1 = -0.5, h_2 = 1.45$; (d) $h_1 = -0.5, h_2 = 1.46$; (e) $h_1 = -0.5, h_2 = 1.5$; (f) $h_1 = -0.5, h_2 = 1.54$; (g) $h_1 = -0.5, h_2 = 1.6$.

dition $\left\|\omega^{n+1}-\omega^{n}\right\|_{\infty}/\left\|\omega^{n+1}\right\|_{\infty} < 10^{-7}$ holds for each sub-region. In each iteration step, the new value of stream function-vorticity is obtained with the relation $\phi^{k+1}(i,j) = \phi^{k}(i,j) + \gamma R^{k}(i,j)$, where $R^{k}(i,j)$ is the residual term, $\phi^{k}(i,j)$ is the problem primitives at mesh point (i,j) in the kth iteration, γ is a relaxation parameter. The value of the relaxation parameter is taken as $\gamma = 2.5 \times 10^{-5}$ by trial and error. This algorithm is coded in the MATLAB version R2022a and the visualization of the stream function is created in the Tecplot 360 software. The code validation is also established in Fig. 3 for $S = -1$ with the results of Deliceoğlu and Aydın [13].

To verify the grid independence of the proposed method, the norm of stream function ($||\psi||_{\infty}$) are obtained for grid sizes $N = \{20, 25, 30, 35\}$ given in Table 2. The results show that the infinity norms of the stream function values are consistent across all tested grids. So, the aspect ratio of the cavity and step size in the sub-regions are fixed $h_1 = -0.2$, $h_2 = 0.8$ and $N = 25$, $N^* = 13$, respectively, in all computations. Different types of flow patterns and bifurcations are generated in the cavity with stationary Reynolds number ($Re = 100$) and moderate Hartmann number (M) for both case $S = -1$ and $S = 1$.

Table 2. The variation of the infinity norm of the stream function depends on the grid size

(N, N^*)	$\|\|\psi_1\|\|_{\infty}$	$\|\|\psi_2\|\|_{\infty}$	$\|\|\psi_3\|\|_{\infty}$
$(20, 10)$	0.08890	0.098666	0.051654
$(25, 13)$	0.08887	0.098740	0.051823
$(30, 15)$	0.08882	0.098732	0.051917
$(35, 18)$	0.08876	0.098655	0.051944

5.1 Benchmark results for divided lid-driven cavity

Before the calculations, it is necessary to determine the RBF parameters required for the method such as the degree of PHS, the highest degree of polynomial in augmentation, and the number of points lying stencil. In theory, one node is required for each polynomial. However, this causes the singularity of the matrix (6), [24, 25]. Therefore, the stencil size is considered to be twice the number of polynomial terms, as suggested by Flyer *et al.* [25]. Throughout the paper, the weights for the Laplacian operator (∇^2) are calculated using the MATLAB code given in [25].

To establish RBF parameter, the method is employed to lid-driven square cavity which is divided into two regions $\Omega_{1,2}$ with the boundary Γ as shown in Fig. 1b. A uniformly distributed node layout is taken; hence the mesh size for each sub-region is given as 25×50. Also, the coupled equations (2)-(3) transform into the Navier-Stokes equations in the absence of a magnetic field ($M = 0$) and are solved iteratively.

Table 3. Results of ψ at the center (ψ_c) and ω at the middle of lid ω_{lid} for $Re = 100$

		PHS r^3			PHS r^5			PHS r^7		
p	n	time	ψ_c	ω_{lid}	time	ψ_c	ω_{lid}	time	ψ_c	ω_{lid}
1	6	11.39s	-0.063927	-9.5212	12.14s	-0.068128	-3.5924	11.53s	-0.063632	-6.6842
2	12	11.58s	-0.065159	-6.7567	11.55s	-0.065205	-6.6982	11.55s	-0.065228	-6.6570
3	20	11.52s	-0.065249	-6.6851	11.54s	-0.065237	-6.6834	11.62s	-0.065228	-6.6808
4	30	11.62s	-0.065223	-6.6888	11.68s	-0.065224	-6.6932	11.61s	-0.065224	-6.6945
5	42	11.64s	-0.065223	-6.6971	11.63s	-0.065225	-6.7023	11.83s	-0.065226	-6.7037

In Table 3, the benchmark results of the stream function in the center domain (ψ_c) and the vorticity in the middle of the lid (ω_{lid}) for $Re = 100$ are shown. The results are compared with those obtained by Luchini [29]. He presented a new discretization scheme and gave $\psi_c = -0.06415$ and $\omega_{lid} = -6.822$ with 41×41 the total number of points for the second-order central difference scheme. Then he obtained $\psi_c = -0.066545$ and $\omega_{lid} = -6.5636$ as extrapolated values. It is clear that the results are consistent.

Table 3 shows that the CPU times required for the solution are quite close. There is no specific change in time, depending on the size of the stencil and the degree of PHS and polynomial. In addition, an increase in the degree of PHS has a small effect on the solution. The closest case to the results of Luchini [29] at any degree of PHS is the third-order polynomial with the stencil size of 20. Flyer *et al.* [24] also stated that with low-order polynomial augmentation stencil size improves accuracy but not convergence rate. Therefore, the calculations use the third-order PHS (r^3) augmented with polynomial terms up to order three ($p = 3$), but the stencil size is chosen to be three times the number of polynomial terms ($n = 30$) for the L-shaped.

5.2 Case 1: Double lids in the opposite direction ($S = -1$)

In Fig. 4, flow patterns are presented in the case at which lids moving in opposite. For cases $M = 25$ and $\alpha = 0°$, the flow within the cavity exhibits three center-type stationary points. Two of them near the top and bottom walls rotate clockwise due to the lids effect, while the other one at the center rotates counterclockwise. When $M = 50$, the vortex in the middle undergoes a transformation: it splits into two saddles with a center due to the cusp bifurcation. By gradual increase of the Hartmann number, when $M = 100$, the number of center-type stationary points in the cavity reaches five. It is observed that when the angle of the magnetic field is $\alpha = 45°$, the effect of the magnetic field decreases. In fact, a separatrix structure is observed with a saddle-type in the middle of the cavity and center points near the

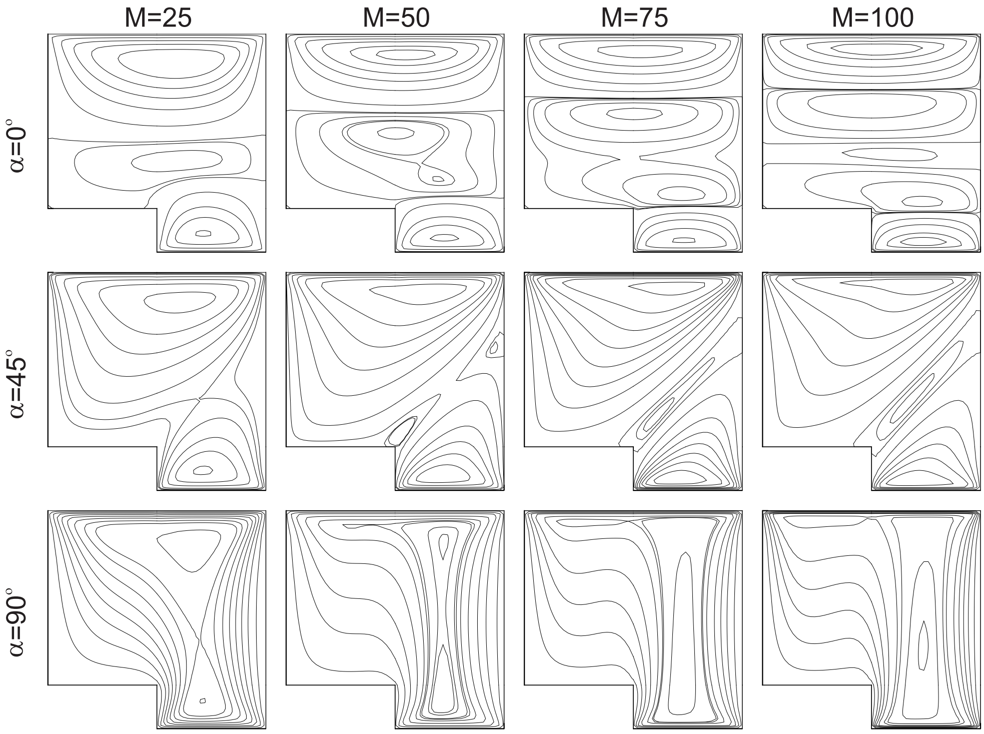

Fig. 4. Stream function contours in the cavity under the magnetic field with $Re = 100$ for $S = -1$.

lid. As the Hartmann number enhance, separation bubbles appear around the corner and on the right fixed wall. By the influence of the magnetic field, vortex formation around the step occurs under the global and cusp bifurcations. Applying the magnetic field to the flow field at $\alpha = 90°$ results in a large separatrix structure as $\alpha = 45°$. However, in this scenario, the upper stagnation point almost aligns with the lower moving lid, and as the magnetic field effect intensifies, the impact of the step and the cover on the flow diverges: streamlines aligned with the lower lid tend to straighten longitudinally, whereas stream lines aligned with the step straighten transversely.

The influence of Re on flow bifurcation is also analyzed. Fig. 5a indicates streamlines for the variations of Re and M for $\alpha = 0°$. In the absence of the magnetic field ($M = 0$), augmentation of Re changes the flow topology. Indeed, cusp bifurcation occurs about $Re = 500$ and bubble creation is generated on the right wall. The main vortex of the flow goes to the center of the cavity. On the other hand, the secondary vortex enlarges with an increase in Re. However, the flow bifurcation remains the same for a high Hartmann number ($M = 50$) since the Lorentz force dominates the effect of Re.

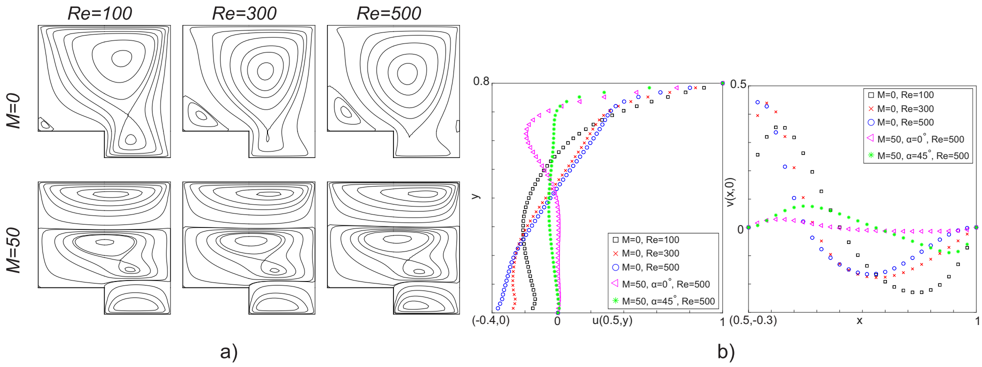

Fig. 5. Impacts of Re and M on a) streamlines b) $u - v$ profiles for $S = -1$.

In Fig. 5b, u and v velocities profiles are plotted along $x = 0.5$ and $y = 0$ for different values of Re, M and α. As seen, u attains the lowest minimum value at $Re = 500$, $M = 0$ since the increase in Re causes the enlargement of the secondary vortex. When the magnetic field effect is taken into consideration, the impact of Re diminishes and u velocity becomes almost zero along $x = 0.5$. In the v velocity profiles, the maximum and minimum values are altered due to the formation of vortices. v velocity values decrease regardless of the direction of the magnetic field. However, the flattening tendency effect is more pronounced with a diminishing inclination angle. A horizontally applied magnetic field causes the v values to be zero along $x = 0$.

Figure 6 depicts the impact of Hartmann number on the vorticity contours for a fixed $Re = 100$ and $\alpha = 0°$. In the absence of the magnetic field, the flow is characterized by strong rotational zones near the top and bottom lids. The interaction between opposite lids causes more complex and asymmetric vorticty lines. An increase in the Hartmann number results in damped vorticity distribution and leads to smoother and more stable flow lines resulting vortex zones.

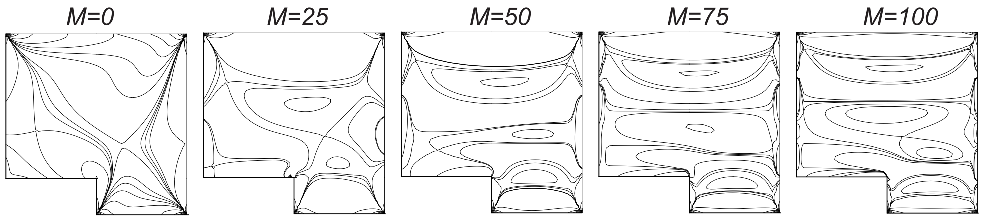

Fig. 6. Vorticity contour for $S = -1$ with fixed $Re = 100$.

5.3 Case 2: Double lids in the same direction ($S = 1$)

For $S = 1$, streamlines associated with flow patterns formed under the magnetic field are exhibited in Fig. 7. The cavity contains two vortices rotating in opposite directions relative to each other for $M = 25$ and $\alpha = 0°$. As the magnetic field strength increases, $M = 100$, the flow motion slows down and the number of vortices through the domain increases as in $S = -1$. The separation line near the corner separates the oppositely moving vortices when the angle between the magnetic field and the flow region is $45°$. With the gradual increase in M, the vortices in the flow get closer to the moving lids, as in the previous case. However, although the effect of the magnetic field is the same for $S = -1$ and $S = 1$, the effect on the streamline topology is different. Indeed, for $\alpha = 45°$, the vortex formation process is started with the separation bubble near the corner in the previous case, whereas a cusp bifurcation is occurred for $S = 1$. In addition, although the topological structure of the flow is the same as for $\alpha = 90°$ with $\alpha = 45°$, as the magnetic field strength increases, a successive nested cusp bifurcation appears at the centre-stagnation point close to the

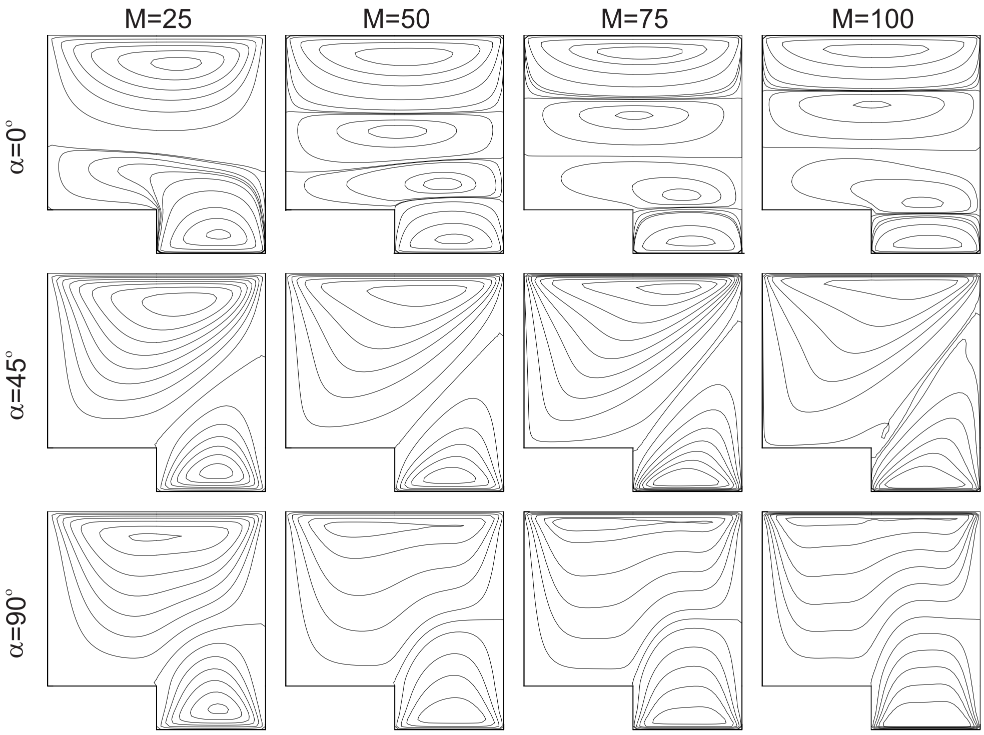

Fig. 7. Stream function contours in the cavity under the magnetic field with $Re = 100$ for $S = 1$.

upper lid.

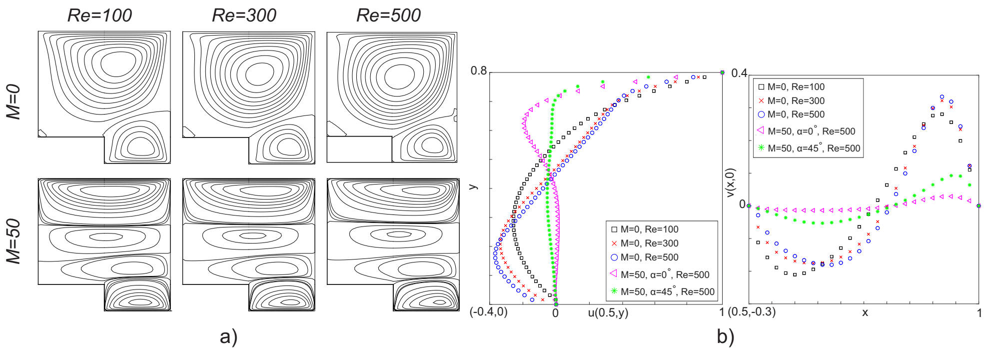

Fig. 8. Impacts of Re and M on a) streamlines b) $u-v$ profiles for $S=1$.

The impacts of Reynolds and Hartmann numbers on the streamlines are also examined for $S=1$ in Fig. 8a. It is observed that the increase in Re does not have an important impact on the flow bifurcation, contrary to the case of $S=-1$. As the Reynolds number rises, the center of the vortices near the moving top and bottom walls shift.

Figure 8b shows the velocity profiles for several values of Re, M and α. The impacts of the physical parameters are the same as in the results for $S=-1$. The maximum and minimum values of v occur near the right wall of the cavity and the left wall of the leg of the cavity instead of the left wall and the right wall, respectively, due to the direction of movement of the bottom wall ($S=-1,1$).

In Fig. 9, the variation of the strength of the horizontally applied magnetic field on the vorticity is illustrated for $Re=100$. For $M=0$, more symmetric vorticity contours are observed compared to results in the case of $S=-1$ in Fig. 6. It is shown that the direction of the moving lid plays an important role in the complexity of the vorticity contours. Due to the increase in Hartmann number and decrease in velocity of the fluid, vortex zones become apparent as in $S=-1$. The impact of the magnetic field on the equivorticity lines is similar to the case of $S=-1$ since the

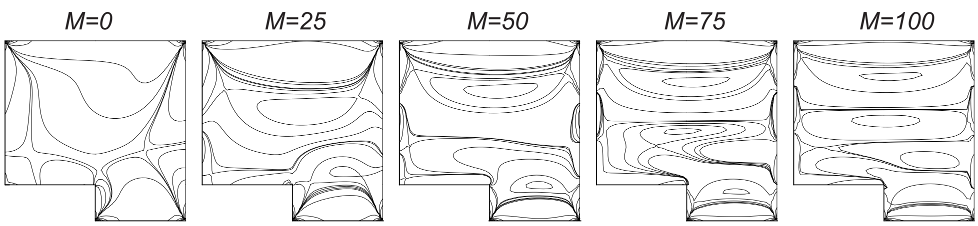

Fig. 9. Vorticity contours in the cavity under the magnetic field with $Re=100$ for $S=1$.

Lorentz force suppresses the rotational motion and damps the vorticity.

6 Conclusion

This study examined that the influences of the strength and the direction of the magnetic field on the flow bifurcation in L-shaped cavity which has a double lid using a numerical method with improvement. The derivative operator at the interface points is approximated by more points contributing to the derivative, and these contributions are found using RBF-FD. Numerical scheme is employed to depict the streamlines and velocity profiles for the variations of Re, M and α. It is reported that the Hartmann number and the inclination angle of the magnetic field play an important role in the classification of the stagnation points by modifying the quantity, location, and nature of critical points in both cases ($S = -1, 1$). However, a slight increase ($Re < 500$) in the Reynolds number does not alter the flow topology in an L-shaped cavity with the same direction of movement. It is also seen from the $u - v$ velocity profiles that the magnetic field reduces the effect of the Reynolds number. In addition, the retardation impact on the flow is more pronounced for the application of a horizontal magnetic field.

References

[1] C.Y. Perng, R.L. Street (1991) A coupled multigrid-domain-splitting technique for simulating incompressible flows in geometrically complex domains. *International Journal for Numerical Methods in Fluids* **13**(3) 269-286.

[2] M. Hriberšek, L. Škerget (2005) Boundary domain integral method for high reynolds viscous fluid flows in complex planar geometries. *Computer Methods in Applied Mechanics and Engineering* **194**(39) 4196-4220.

[3] S. Yeasmin, M. Billah, M.Z. Molla, K. Hoque (2022) Numerical analysis of unsteady mixed convection heat transfer characteristics of nanofluids confined within a porous lid-driven L-shaped cavity. *International Journal of Thermofluids* **16** 100218.

[4] B. Alshuraiaan (2023) Fluid structure interaction analysis of natural convective flow and heat transfer in an L-shaped cavity. *Journal of Advanced Research in Fluid Mechanics and Thermal Sciences* **109**(1) 1-12.

[5] A. Marafie (2023) Natural convection flow and heat transfer in an L-shaped cavity partially filled with porous medium: numerical analysis. *Journal of Porous Media* **26**(7) 1-15.

[6] P.R. Kanna, A. Satheesh, S.K. Arumugam, H.F. Öztop, N.R. Devi (2025) Double-diffusive natural convection in L-shaped cavity by lattice Boltzmann method: Numerical study. *Heat Transfer Engineering* **46**(15) 1418–1432.

[7] M.B.B. Hamida (2025) Investigation of fluid-structure interaction and heat transfer dynamics in a wavy L-shaped enclosure with an elastic baffle. *International Communications in Heat and Mass Transfer* **162** 108617.

[8] F. Selimefendigil, H.F. Öztop (2019) MHD mixed convection of nanofluid in a flexible walled inclined lid-driven L-shaped cavity under the effect of internal heat generation *Physica A: Statistical Mechanics and its Applications* **534** 122144.

[9] T. Armaghani, M. Sadeghi, A. Rashad, M. Mansour, A.J. Chamkha, A. Dogonchi, H.A. Nabwey (2021) MHD mixed convection of localized heat source/sink in an Al_2O_3-Cu/water hybrid nanofluid in L-shaped cavity. *Alexandria Engineering Journal* **60**(3) 2947-2962.

[10] K.B. Saleem, A.H. Marafie, K. Al Farhany, W.K. Hussam, G.J. Sheard (2023) Natural convection heat transfer in a nanofluid filled L-shaped enclosure with time-periodic temperature boundary and magnetic field. *Alexandria Engineering Journal* **69** 177-191.

[11] N.Z. Khan, S. Bilal, L. Kolsi, A. Shflot, M. Malik (2024) A case study on entropy generation in MHD nanofluid flow in L-shaped triangular corrugated permeable enclosure. *Case Studies in Thermal Engineering* **59** 104487.

[12] N.Z. Khan, N. Tahir, A. Shflot, M. Malik (2025) Entropy generation and heat transfer in MHD free convection within L-shaped cavities: A computational and AI-based approach. *Results in Engineering* **26** 104659

[13] A. Deliceoğlu, S. Han Aydin (2013) Flow bifurcation and eddy genesis in an L-shaped cavity. *Computers & Fluids* **73** 24-46.

[14] A. Deliceoğlu, S. Han Aydin (2014) Topological flow structures in an L-shaped cavity with horizontal motion of the upper lid. *Journal of Computational and Applied Mathematics* **259** 937-943.

[15] A. Deliceoğlu, D. Bozkurt, E. Çelik (2020) Flow topology in an L-shaped cavity with lids moving in the same directions. *Mathematical Methods in the Applied Sciences* **43**(15) 8317-8326.

[16] S.R. Bhopalam, D.A. Perumal (2020) Numerical analysis of fluid flows in L-shaped cavities using lattice Boltzmann method. *Applications in Engineering Science* **3** 100016.

[17] X.-L. Cheng, A.W. Shaikh (2006) Iterative methods for the poisson equation in L-shape domain based on domain decomposition method. *Applied Mathematics and Computation* **180**(1) 393-400.

[18] C. Chniti, F. Nataf, F. Nier (2009) Improved Interface Conditions for 2D Domain Decomposition with Corners: Numerical Applications. *Journal of Scientific Computing* **38**(2) 207-228.

[19] C. Chniti (2017) Optimized interface conditions in domain decomposition methods to solve reaction–diffusion problems with strong heterogeneity in the coefficients in a sectorial domain. *Applied Numerical Mathematics* **118** 117-130.

[20] E. Çelik, M. Gurbuz-Caldag (2024) Solution of MHD-Stokes flow in an L-shaped cavity with a local RBF-supported finite difference. *Engineering Analysis with Boundary Elements* **158** 356–363.

[21] H. YOSINOBU, T. KAKUTANI (1959) Two-dimensional Stokes flow of an electrically conducting fluid in a uniform magnetic field. *Journal of the Physical Society of Japan* **14**(10) 1433-1444.

[22] U. MÜLLER, L. BÜHLER (2013) "Magnetofluiddynamics in Channels and Containers". Springer Berlin Heidelberg, Berlin.

[23] G.E. FASSHAUER (2007) "Meshfree Approximation Methods with MATLAB". WORLD SCIENTIFIC, Singapore.

[24] N. FLYER, B. FORNBERG, V. BAYONA, G.A. BARNETT (2016) On the role of polynomials in RBF-FD approximations: I. interpolation and accuracy. *Journal of Computational Physics* **321** 21-38.

[25] N. FLYER, G.A. BARNETT, L.J. WICKER (2016) Enhancing finite differences with radial basis functions: Experiments on the Navier-Stokes equations. *Journal of Computational Physics* **316** 39-62.

[26] V. BAYONA, N. FLYER, B. FORNBERG, G.A. BARNETT (2017) On the role of polynomials in RBF-FD approximations: II. Numerical solution of elliptic PDEs. *Journal of Computational Physics* **332** 257-273.

[27] M. BRØNS, J.N. HARTNACK (1999) Streamline topologies near simple degenerate critical points in two-dimensional flow away from boundaries. *Physics of Fluids* **11**(2) 314-324.

[28] J.N. HARTNACK (1999) Streamline topologies near a fixed wall using normal forms. *Acta Mechanica* **136**(1) 55-75.

[29] P. LUCHINI (1991) Higher-order difference approximations of the Navier-Stokes equations. *International Journal for Numerical Methods in Fluids* **12**(5) 491-506.